Earth Surface Processes and Landforms
June 2022, Volume 47, Issue 8, Pages 2024-2043
https://doi.org/10.1002/esp.5361
https://archimer.ifremer.fr/doc/00755/86687/

Catastrophic overwash and rapid retreat of a gravel barrier spit during storm events (Sillon de Talbert, North Brittany, France)

Suanez Serge [1, *], Stéphan Pierre [1], Autret Ronan [1, 2], Houron Julien [3], Floc'h France [4], David Laurence [1], Ammann Jérôme [4], Accensi Mickael [5], André Gael [6], Le Guyader Damien [7], Cancouët Romain [8]

[1] LETG UMR 6554 CNRS Université de Bretagne Occidentale, Institut Universitaire Européen de la Mer, rue Dumont d'Urville Plouzané, France
[2] Laboratoire de Dynamique et de Gestion Intégrée des Zones Côtières, Chaire de Recherche en Géoscience Côtière Université du Québec à Rimouski Rimouski, QC , Canada
[3] Réserve naturelle régionale du Sillon de Talbert, 48 Rue du Sillon de Talbert Pleubian, France
[4] Laboratoire Géosciences Océan, LGO UMR 6538 CNRS Université de Bretagne Occidentale, Institut Universitaire Européen de la Mer, rue Dumont d'Urville Plouzané, France
[5] Laboratoire d'Océanographie Physique et Spatiale, LOPS UMR 6523, Ifremer/CNRS/UBO/IRD, Z.I. Pointe du Diable, CS 10070 Plouzané, France
[6] Service Hydrographique et Océanographique de la Marine, 13 rue du Chatellier, CS 92803 Brest, France
[7] Geo4Seas Society, 3 Venelle de la Tour d'Auvergne Le Relecq-Kerhuon , France
[8] EURO-ARGO ERIC, Campus Ifremer, Technopole Brest Iroise, 1625 Route de Sainte-Anne Plouzané ,France

* Corresponding author : Serge Suanez, email address : serge.suanez@univ-brest.fr

Abstract :

The morphodynamic functioning of the Sillon de Talbert gravel barrier spit is analyzed using a high-frequency survey carried out between September 2012 and December 2019. It is based on beach profile measurements along two transects, modeling offshore wave data (WW3), tide gauge records, and shallow waves and water levels recorded in the intertidal zone. A barrier retreat of –23 to –30 m over the 7-year survey (i.e., –3.3 to –4.3 m.y-1) is measured. This retreat is not related to long-term SLR (macroscale of 102 to 103 yr), but to mesoscale (100 to 102 yr) morphogenic events combining storm wave and high spring tide. Over 87% to 90% of the barrier retreat is due to three significant events (February 1-2, 2014, February 9, 2016, and January 3, 2018). The storm impact scale model of Orford and Carter (1982) is tested. The estimation of the wave runup for the calculation of extreme water levels (i.e., peak overflow elevation (Oe) component), is based on the calibration of an equation performed from in situ measurements of the swash elevation. The flow depth (Od,q) overtopping the crest of the barrier (Bh) is thresholded by taking into account the morphological response of the barrier in order to define regimes corresponding to overtopping, discrete overwash, and sluicing overwash. While the Orford and Carter model is generally successful in reproducing the morphodynamic evolution of the Sillon de Talbert, the wave energy flux (F) must be considered as an additional parameter in order to improve the fit of the model, so far as it contributes in some cases to change the morphodynamic regime. Thus, the wave

energy flux constitutes a key component in the quantification of the water flow across the barrier (Od,q) corresponding to the hydrodynamic forcing of the model, which becomes (Od,F).

1. Introduction

Gravel-dominated barrier spits presenting a single-crested ridge are highly sensitive to landward migration due to cross-shore dynamics associated with rollover processes. This barrier retreat is the main morphological response to relative sea-level rise (SLR) operating over different timescales from microscale to megascale. Orford et al. (1995a) defined appropriate timescales for the analysis of the rate of sea-level rise in the study of gravel-barrier retreat; they extend from microscale ($<10^0$ yr), to mesoscale (10^0 to10^2 yr), to macroscale (10^2 to 10^3 yr), and finally to megascale ($>10^3$ yr). In addition, subdivisions for mesoscale specification span across inter-annual (1 to 5 yr), to sub-decadal (5 to 10 yr), culminating in decadal (10^1 to 10^2 yr) timescales. Orford and Carter (1995) distinguished (*i*) microscale ($<10^0$ yr), controlling the rise of water level due to storm events associated with barrier crest overtopping and overwashing that lead, respectively, to reduced and accelerated barrier retreat, and (*ii*) macroscale (10^2 yr), governing secular sea-level rise that influences the rhythm of coastal retreat by controlling the rate at which the coastal erosion front passes across the terrestrial basement. As indicated by Orford et al. (1995a, 1996), the mesoscale (10^0 to 10^2 yr) rather than the macroscale ($>10^2$ yr) SLR rate is the critical control on barrier retreat, as mesoscale sea-level variation in combination with storm surge potential is able to rapidly raise water levels to the elevation threshold sufficient for barrier overwash and hence drive barrier retreat due to rollover.

Significant rollover processes occur during extreme events when wave runup overtop, overwash, or strongly inundate the crest of the barrier over a very short time-period (*i.e.*, microscale $<10^0$ yr) (Matias et al., 2012; Masselink and van Heteren, 2014; Brown et al., 2019; Phillips et al., 2020; Pollard et al., 2021). The most effective storm-impact scaling model describing the response of the barriers to storms was proposed by Orford and Carter (1982). It is based on the elevation difference between the peak overflow elevation (O_e) and the height of the barrier crest (B_h), which is known as "freeboard" (Orford and Carter, 1982; Orford and Anthony, 2011) (Figure 1). O_e corresponds to the extreme water level (EWL), also corresponding to the maximum runup elevation R_{high}. Therefore, this parameter is calculated as follow:

$$O_e = \text{EWL} = R_{high} = tide + surge + runup\ (\eta + R) \qquad [1]$$

where *runup* is the sum of wave setup (η) and swash elevation (R).

Depending on the water flow across the barrier ($O_{d,q}$), where d is the water depth, and q the volumetric discharge, morphological responses of the barriers to storm impact are ranged into four distinct regimes: *swash overtopping*, *discrete overwash*, *sluicing overwash*, and *catastrophic overwash/breaching* (Orford and Anthony, 2011) (Figure 1). *Swash overtopping* occurs when the peak overflow elevation reaches the top of the barrier without crest overwashing (*i.e.*, positive to neutral freeboard), inducing an accretion of the crest due to the infiltration of the uprush reaching the crest without efficient backwash. Then, as the swash runup elevation increases, overwashing processes become more destructive. The discrete *"overwash*" induces a slight erosion of the crest when wave runup passes over it. The "*sluicing overwash*" process completely removes the top-barrier due to an energetic and unidirectional flow that is largely unaffected by percolation. In some cases, the lowering of the crest due to erosion is related to deposition of small-scale back-barrier washover fans. The last regime,*"catastrophic overwash",* occurs during intense storms generating extreme sea-level increases. Overflow induces a strong erosion of the complete barrier in the form of a breach or throat, and washover fans and splays are deposited on the back-barrier. This latter extreme storm-impact regime leads to intense landward barrier retreat and/or barrier breaching which generally corresponds to the final "catastrophic step" of significant long-term rollover processes (Carter and Orford, 1993; Orford et al., 1996, 2002). The use of this model is therefore strongly dependant on the evaluation of the swash runup elevation for estimation of the peak overflow elevation (O_e), which also corresponds to extreme water level (EWL). This component is the key parameter controlling the occurrence of gravel barrier overwashing (Matias et al., 2012; Masselink and van Heteren, 2014). In contrast to sandy beaches (*e.g.*, Stockdon et al., 2006), only a few recent studies of wave runup estimation based on field-runup have been carried out on steep gravel beaches or barriers (Powell, 1990; Polidoro et al., 2013; Poate et al., 2016; Didier et al., 2020).

According to the Davis (1972) classification, gravel barriers are often divided into two types, drift-aligned and swash-aligned. This distinction is based on the plan view geometry of the barrier and its morphodynamic relationship to longshore sediment scarcity for a swash-aligned barrier, and significant surplus of longshore sediment transport for a drift-aligned barrier. Many studies based on eastern Canadian and northwest European data have established the nature of the swash-aligned gravel barrier response to SLR at the mesoscale (Orford et al., 1991; Forbes et al., 1991; Carter and Orford, 1993; Orford et al. 1995b, 1996). In this paper we examine the cross-shore morphological dynamics of the gravel spit of the Sillon de Talbert a swash-aligned barrier (Stéphan et al., 2012) that has been evolving to a drift-aligned barrier during the last few decades (Suanez et al., 2018a). This study is based on a high frequency beach profile survey which has been ongoing since September 2012. It consists of weekly to monthly topo-morphological measurements along two transects situated on the most retreating zones of the spit. This survey is also based on hydrodynamic *in situ* measurements (waves and water levels) using pressure sensors and WW3 wave modelling. The morphological changes of the spit related to cross-shore dynamics are addressed using the storm-impact model of Orford and Carter (1982). The calculation of the runup (R) -as a main component of the height of the extreme water level (EWL)- was based on the calibration of the existing empirical formula of Hunt (1959), modified by Battjes (1974). The parametrisation of this equation was based on the field measurements of the wrack lines related to the highest high-tide runup elevation and the analysis of morphosedimentary and hydrodynamic conditions, following the methods of Cariolet and Suanez (2013) and Suanez et al. (2015).

2. Study site

The gravel barrier spit of the Sillon de Talbert is located on the northern Brittany coast (France) in the department of *Côtes d'Armor* (Figure 2). The morphological setting of this gravel barrier spit has been detailed by Stéphan et al. (2010, 2012, 2018), and Suanez et al. (2018a). The gravel barrier spit of the Sillon de Talbert is driven by both longshore and cross-shore dynamics. However, since sediment transfers due to cross-shore dynamic are dominant comparing to longshore sediment transferts (430,000 m^3 *vs* 52,000 m^3 between 2002 and 2019) (Suanez et al., 2020), the Sillon de Talbert is considered as a single-ridge swash-aligned barrier that stretches over 3.5 km long. It is composed of a mixture of sand and gravel sediment with an estimated volume of 1.23 10^6 m^3. On the distal part of the spit, the sandy fraction decreases, while the gravel sediment significantly increases. The beach face is characterized by a slope break point about 1 m above the mean water level, delimiting the spit accumulation from the large flat rocky platform (0.01%). The upper part of the beach face shows steeper slopes of between 5% and 15%. According to the morphological and sedimentary features, Stéphan et al. (2012) have subdivided the barrier into four distinct morphosedimentary units, from Unit 1, corresponding to the proximal sandy dune section, to Unit 4, forming the distal section (Figure 3a). These two sections are the most stable in terms of shoreline dynamics. This is due to *(i)* the coastal defence structures (*i.e.*, rip-rap and groin) remaining on Unit 1 preventing erosion processes, and *(ii)* the longshore sediment transport that supplies the distal part of the spit (*i.e.*, Unit 4) inducing significant accretion and enlargement of this section. These two sections – Units 1 and 4– are characterized by crest heights reaching 8.5 m to 9.5 m above sea level (a.s.l.), respectively. Conversely, both Units 2 and 3, corresponding to the proximal gravel section and the median section, respectively, have displayed the most retreat in the last 80 years (Stéphan et al., 2012; Suanez et al., 2018a). The crest height is about 7 m a.s.l. for Unit 2, and 7.5 m a.s.l. for Unit 3.

This coastal area is located in a macrotidal to megatidal environment with a maximum tidal range of 10.95 m (SHOM, 2016). The most frequent swells come from the WNW with a resultant vector of around 302° (Figure 2d). Consequently, the waves break with a slight angle according to the coastline's orientation (□54°). This non-parallel swash alignment (□>0) generates a longshore drift oriented to the NE. Modal heights (H_{m0}) of deep sea waves are between 1 and 1.5 m and modal periods (T_{pic}) are between 9 and 10 seconds. During storms, wave heights can reach 9 m with periods of 20 seconds.

Based on the analysis of ancient maps (Stéphan et al., 2012), the long-term morphological evolution of the Sillon de Talbert indicates that up to the end of the 17th century it was connected to the islets of the Olone archipelago located in the NE. The detachment of the barrier occurred in the early 18th century and gave rise to a 3.2 km long gravel spit (Stephan et al., 2012). This is probably due to the severe storm event of November 26, 1703, which was one of the most extreme events recorded along the south England and northwest French coasts over the past few centuries (Lamb and Frydendahl, 2005). The transformation from anchored barrier to barrier spit triggered an alongshore drift sediment transport that was associated to *(i)* a slight longshore cannibalization process, which increased throughout the 19th and 20th centuries due to sediment depletion, and *(ii)* a "cross-shore" landward displacement by rollover facilitated by the disconnection. Using the back-barrier edge (see Figure 1b) Pinot (1994) estimated long-term (1775-1966) rate of spit retreat at –0.5 $m.yr^{-1}$. Stéphan et al. (2012) have shown same estimation of average landward migration rate up to –1.1 $m.yr^{-1}$ between 1930 and 2010, and they highlight the inefficiency of the longshore 1,400 m long riprap, installed from the mid-70's to the beginning of the 80's, in preventing the retreat of the barrier spit (Figure 3d). More recently, Stéphan et al. (2018) and Suanez et al. (2018a) demonstrated that this rate

has increased for the last fifteen years (2002-2017), reaching –2 m.yr^{-1}, with a maximum spit migration up to –150 m on the median section, and –160 m on the gravel proximal section (Figure 3a), where a breach opened in March 2018 (Figure 3e).

Suanez et al. (2018a) indicated that storm events combined with high spring tide levels control more than 95% of this retreat due to catastrophic overwash/inundation processes (Figure 3b and 3c). This was the case during the Johanna storm of March 10, 2008 when the maximum spit retreat reached –22 m (Stéphan et al., 2010). It was also the case during the stormy winter of 2013-2014 when the maximum spit retreat reached –30 m (Blaise et al., 2015). Figure 3b illustrates the overwashing of the section (*i.e.*, Unit 1) where the crest height is one of the highest (*i.e.*, 8.5 m to 9 m a.s.l.).

3. Data and methods

3.1. Beach profile measurements

The monitoring of topo-morphological changes is based on two beach profile measurements carried out between September 2012 and December 2019 along two transects situated on both spit sections where retreat rates are the most significant (Figure 4). These sections correspond to Unit 2 (proximal gravel section) and Unit 3 (median section) (see Figure 3a). This survey was performed at a weekly to monthly frequency using a Leica tacheometer TCR303 and DGPS Topcon HiperV (Suanez et al., 2018b). A total of 116 and 119 profiles were measured on transects A and B, respectively. Each measurement was calibrated using the geodesic marker from the French datum and the geodesic network provided by the IGN (*Institut Géographique National*). The position of the control points was measured to estimate the margin of error reaching ± 5 to 7 cm in *x*, *y*, and ± 2 cm in *z*. Beach profile measurements were used to monitor the morphological changes of the spit, such as *(i)* the crest lowering/elevation (Δh_{crest}) and the crest horizontal displacement (Δx_{crest}), *(ii)* the spit back-barrier landward retreat (Δr_{spit}), and *(iii)* the seaward beach face slope ($tan\square$) corresponding to the swash zone. It was calculated on the section of the beach profile defined by the crest of the barrier as the upper bound, and the base of the barrier front (break point between the platform and the seaward beach face) as the lower bound. In addition, quantification of the changes in sediment budget was measured for the three sections of the profile, *i.e.*, the beach face, the crest, and the back-barrier, in order to analyze the sediment transport due to overtopping, discrete and sluicing overwashing processes, respectively. The distinction between these three sections is based on the consideration of morphological breaks in the slope.

In July 2014, a granulometric and sedimentological analysis was performed along both profiles A and B (Fichaut et al., 2015). This work was based on sediment samples taken at the surface and at depth when the characteristics of the latter were different from those at the surface, especially in terms of the share of sandy sediments compared to coarse sediments (gravels and pebbles).

The sandy fraction is always significant along profile A, except on the back-barrier where it is absent on the surface. It represents between 30% and 60% of the sedimentary material (Figure 4e). The sandy material is largely dominant at the top of the beach face where it is frequently removed by the wind and feeds the embryo dunes located at the top of the barrier. These results are in agreement with earlier work by Morel (1998), and confirmed by Stéphan et al. (2012) to justify the morphosedimentary compartmentalization of the barrier. The authors indicated that this section (*i.e.*, proximal section as Unit 2, see Figure 3a) is

characterized by a heterogeneous mixture of poorly sorted sand and pebbles representing less than 40% of the material. In contrast, profile B shows a completely different sediment grain size distribution. The coarse fraction (gravels and pebbles) represents the majority of the surficial sediment along this profile. The sandy fraction, a much lower proportion (about 10%), is encountered only at depth of about 0.15 m, essentially on the sea-face beach (Figure 4f). This grain size distribution gives this section of the barrier a greater permeability because the interstitial voids are not filled with fine sediments. These sedimentological characteristics were also described by Morel (1998) and Stéphan et al. (2012), indicating that the median section of the barrier (Unit 3, see Figure 3a) was primarily coarse sediment (>70%).

3.2. Hydrodynamic analysis: data acquisition and methods

3.2.1 Offshore wave modeling

Offshore wave data between 01/09/2012 and 31/12/2019 were obtained from the HOMERE hindcast data set (Boudière et al., 2013). This hindcast uses the WAVEWATCH III V4.18 spectral model (Tolman et al., 2014; Roland and Ardhuin, 2014) and the NORGAS-UG configuration. This configuration was implemented with unstructured and higher resolution grids on the coastal zone, thus enabling the reproduction of the wave climate in the shallow zone. It was forced by the wind fields from the CFSR reanalysis with a resolution ranging from 0.25° to 0.5° (Saha et al., 2010) and by the surface currents generated from an atlas of harmonic tidal constituents obtained from outputs of the MARS circulation model (Lazure and Dumas, 2008). The present dataset corresponds to coordinates 3.047°W, 48.927°N, at a depth of about –50 m, node #65681 (Figure 2b).

Wave parameters such as direction (D), wave height (H_{m0}), and period ($T_{m0,-1}$) were extracted for the analysis of offshore wave conditions. To produce a clearly identifiable significant extreme storm event threshold, the 0.01% exceedance (99.9th percentile) wave height is calculated (Grieco and DeGaetano, 2019). A threshold of about 5 m (5.07 m precisely) was obtained using the 7-year data set. The wave energy flux, F, of these major events was calculated using (see Barnard et al., 2017):

$$F = \frac{\rho g^2 H_{m0}^2 T_{m0,-1}}{64\pi} \qquad [2]$$

where F is expressed per unit crest length of the wave (in J.m^{-2}), ρ = 1,025 kg.m^{-3} is the density of seawater, g = 9.81 m.s^{-2} is the acceleration due to gravity, H_{m0} is the significant wave height, and $T_{m0,-1}$ is the wave period.

3.2.2 Hydrodynamic records in the shallow zone

The survey was also based on hydrodynamic records (wave and water level) in the shallow zone using an OSSI-010-003C pressure sensor (Ocean Sensor Systems Inc.®, accuracy ± 1.5 cm specification). These records started in September 2012 and are ongoing (Suanez et al., 2018c). The pressure sensor was deployed in the tidal zone along profile B, at –0.461 m a.s.l., which approximately corresponds to the mean sea water level (Figure 4a and 4b). Therefore, the sensor was out of the water twice a day during low tide. A recording frequency of 5 Hz was chosen to reproduce the wave spectrum as accurately as possible.

The OSSI pressure sensor data were corrected *i)* from the atmospheric mean sea level pressure recorded at the Ploumanac'h *Météo France* record station (Figure 2a), and *ii)* the non-

hydrostatic pressure following the linear wave theory (Homma et al., 1966; Bishop and Donelan, 1987). The mean surface elevation (*h*) was extracted using a moving mean over 10 minutes of signal. In order to retrieve the wave spectrum and wave averaged parameters, Fourier transforms of the detrended water level were used. The Fast Fourier Transform method was applied over 1,024 data points (at 5 Hz) for incident gravity wave bands (between 0.04 and 0.4 Hz). Since the signal is not perfectly periodic, leakage issues could induce artifacts in the resulting spectrum. To avoid this, a Hamming window was applied to the signal, leading to zero values at the edges. An average was carried out over several contiguous spectra with 50% overlap. The average was performed over 15 minutes for the incident band (Pierson and Marks, 1952). The mean spectral wave parameters, *i.e.*, signicant wave height H_{m0} and the equivalent spectral mean period $T_{m0,-1}$, were then computed (IAHR, 1989). Following the same method as above, extreme wave height (H_{m0}) events based on 99.9th percentile (up to 1.8 m) were inventoried.

For both the offshore and shallow wave data set, wave parameters such as wave height (H_{m0}) and mean period ($T_{m0,-1}$) recorded at both daily high tide levels were selected for the specific hydrodynamic analysis related to morphological changes. The comparison between the WW3 offshore wave modelling and the OSSI shallow wave records was conducted using linear regression. It shows a good fit with R^2 of 78%, with highest $H_{m0-OSSI}$ reaching about 2 m *vs* 5 m to 6 m for offshore wave heights (H_{m0-WW3}) (Figure 5a). This reflects relevant wave energy dissipation across the large and flat nearshore rocky platform facing the gravel barrier spit.

3.2.3 Tide gauge records from the SHOM

Since there is no tide gauge station on the Sillon de Talbert, data from both daily predicted high tide levels were obtained by modeling at the *Les Héaux-de-Bréhat* lighthouse site (Figure 2b). These data were computed and provided by the French hydrographic body called SHOM (*Service Hydrographique et Océanographique de la Marine*). However, the closest referenced tide gauge station managed by SHOM corresponds to the station of Roscoff located at about 70 km west of the Sillon de Talbert (Figure 2a). The data recorded at this station were used to calculate surge level at the same time of both daily high tide levels mentioned previously. Then, the surge level at Roscoff was added to the predicted tide level obtained at the *Les Héaux-de-Bréhat* site in order to acquire the maximum water level for both daily high tide levels. This approach was the most accurate method for estimating the observed tide level on the Sillon de Talbert, considering there is no tide gauge station in this zone.

The correlation between the SHOM observed tide level and the OSSI water level for both daily high tides was conducted, showing a very good fit (R^2: 97%) (Figure 5b). Therefore, data obtained by the OSSI wave gauge sensor were used to fill the gaps when the SHOM observed tide data were missing, and *vice versa*.

3.3 Maximum swash elevation field measurement

The maximum swash elevation (as a maximum wave runup) was based on the wrack deposit measurement, assuming that this limit corresponded to the highest level reached by wave runup during the previous high tide preceding the measurement (Cariolet and Suanez, 2013; Suanez et al., 2015). Most of the time, the wrack deposit accumulated during the previoust high tide is clearly identifiable because it is wet, and/or its physiognomic aspect is not deteriorated. This indicator was used to quantify *in-situ* environmental conditions and dimensional swash parameters for the best calibration of the runup formula (Plant and

Stockdon, 2015). Then, this runup component was applied to determine the hydrodynamic conditions (*i.e.*, extreme water level) related the storm-impact scaling model of Orford and Carter, (1982) describing the response of the spit barriers to storms as one of four types: overtopping, discrete overwash, sluicing overwash, and catastrophic overwash.

Depending on the meteorological conditions prevailing before the measurement, the limit of the position of the wrack line was either very easy to identify, (Figure 6a and 6b), or completely impossible to identify (Figure 6c). In the later case, while the beach profile was measured, the position of the wrack limit was not. When it was not possible to precisely determine this limit, this uncertainty was recorded during the field measurement process in such a way as to use this information during data processing (Figure 7). When the wrack line overtopped the crest –towards back-barrier– due to overwash processes (Figure 6d), the height of the top of the crest was selected as the maximum swash runup elevation. In this case this information was also used during data processing (Figure 7). As such, it is possible to notice that the number of overwash events was at least twice as great for profile A than for profile B. This is explained by the fact that the height of the spit is lower in that sector of profile A than that of profile B.

The wave characteristics (H_{m0} and $T_{m0,-1}$) associated with these highest levels were calculated on a 2-hour time step around the time of high tide level (1 hour before, and 1 hour after).

When it was not possible to determine and measure precisely the wrack line as the swash limit (*i.e.*, Figure 6c), the uncertainty component was taken into account during data processing by removing the data which were considered outliers. As shown in Figure 8, there is a very good correlation between the observed tide and the height of the swash limit. It should be noted that some data which were qualified as unreliable in the field were retained because they appeared to be consistent. Points below the 1:1 line indicate a negative runup value. These values can be interpreted as the margin of error inherent to the method (□0.2 m). In this case, the wrack line has moved down the profile with the backwash flow, especially at the top of the barrier where the slope is particularly steep.

The amplitude of the swash limit reach 2.5 m to 6.4 m for profile A, against 2.1 m to 7.2 m for profile B. The amplitude of the maximum swash elevation (ΔR_{max} = swash limit – observed tide) is between 1.6 m and 2.2 m for profiles A and B, respectively (Figure 7). Finally, the data indicated that the process of crest overtopping due to *sluicing overwash* or *catastrophic overwash* was twice as frequent on profile A (6 events) than profile B (3 events).

4. Results

4.1. Morphological beach profile changes

The results show very similar evolution along both profiles A and B, characterized by alternating erosive and recovery phases (Figure 9):

(i) a first phase, from September 18, 2012 to December 18, 2013, indicates no significant changes. The variation of the height of the crest (Δh_{crest}) never exceeded ± 20 cm, and its position (see Δx_{crest}) remained very stable, particularly for profile B (Figure 9g). In detail, both envelopes of profiles showed the migration of berms along the seaward beach face characterized by a slope ($tan\beta$) of about 0.10 and 0.16 for profiles A and B, respectively (Figure 9d and 9h).

(ii) a second phase, from the beginning of January 2014 to March 5, 2014, was characterized by significant changes related to severe erosion. During this period, the crest of the barrier spit

lowered by –0.45 m and –1.35 m along profiles A and B, respectively (Figure 9b and 9f), and retreated by about –12 m to –14 m (Figure 9c and 9g). Both envelopes of profiles A and B show an intense erosion of the seaward beach face, and similarly a significant accretion on the back-barrier. These morphological changes took place in three stages; at the beginning of January (see profile 07/01/2014), February (see profile 13/02/2014), and March (see profile 05/03/2014) (Figure 9a and 9e). This evolution illustrated the process of rollover due to catastrophic inundation and erosion leading to a great landward displacement of the barrier spit. Similarly, the slope (*tan*β) of the beach face decreased from 0.10 to 0.07 for profile A, and from 0.16 to 0.11 for profile B (Figure 9d and 9h).

(iii) from April 2014 to December 2017, a third phase was mainly characterized by the elevation of the crest of the barrier spit reaching about +0.44 m at profile A, and +1.1 m at profile B (Figure 9b and 9f). This process of recovery led to the top barrier regaining its pre-storm altitude for both profiles. However, this recovery phase was interrupted by a brief but significant episode of crest lowering on February 12, 2016. The profiles show that the rise of the crest was related to erosion of the beach face (Figure 9a and 9e). Therefore, the part of the sediment eroded to the beach face contributed to the elevation of the crest, inducing an increase of the slope (*tan*β) of the seaward beach from 0.07 to 0.095 for profile A, and from 0.11 to 0.12 for profile B. In terms of barrier spit migration, a significant landward displacement of the crest of about 7 m was experienced principally on profile B as shown by the February 12, 2016 measurement (Figure 9g). Similarly, a net back-barrier landward migration of 8.5 m and 6 m occurred for profiles A and B, respectively (Figure 9a and 9e).

(iv) between December 4, 2017 and January 5, 2018, a major episode of crest lowering and retreat was experienced on both profiles A and B. Crest lowering reached –0.42 m and –1.28 m on profiles A and B, respectively (Figure 9b and 9f), while the retreat of the crest was about –6.25 m and –8 m, respectively (Figure 9c and 9g). This fourth phase was strongly erosive, and once again, the majority of the sediment eroded from the top of the spit was transferred and deposited to the back-barrier, inducing a global landward barrier spit migration of about –5 m to –6 m for both profiles (Figure 9a and 9e). This erosive event was also related to a decrease of the beach face slope on both profiles (Figure 9d and 9h).

(v) a fifth and final phase began after January 5, 2018, until the end of December 2019. It is characterized by the crest elevation reaching +0.32 m and +1.25 m on profiles A and B, respectively (Figure 9b and 9f), while the position of the crest experienced significant progradation of +2 m and +7 m on profiles A and B, respectively (Figure 9c and 9g). Similarly, the slope of the seaward beach face increased from 0.088 to 0.093 and from 0.093 to 0.132 for profiles A and B, respectively (Figure 9d and 9h).

Regarding all the parameters over the entire survey period between September 2012 and December 2019, the crest migration on profile A (*i.e.*, proximal gravel section) and profile B (*i.e.*, median section) indicated that the crest (Δx_{crest}) of the Sillon de Talbert has retreated by about –22 m to –30 m, respectively, while the back-barrier spit retreat (Δr_{spit}) reached about –23 m to –30 m. This landward displacement due to rollover processes represents a migration rate of about –3 to –4 m.y^{-1} over the last 7 years. The variation of crest height (Δh_{crest}) for profile A reached about 0.5 m with a minimum of 6 m and a maximum of 6.5 m. For profile B, it was about 1.9 m with a minimum of 5.7 m and a maximum of 7.6 m. For both profiles, it takes about 12 to 14 months to completely restore the crest height after a major lowering due to crest overwash processes. Such was the case after the stormy winter of 2013-14, the Imogen storm of February 8, 2016, and the Eleanor storm of January 3-4, 2018.

4.2. Hydrodynamic forcing and overwashing processes

Offshore waves display seasonal variations of significant wave height. There was a maximum H_{m0} of 5 m, exceeding the 99.9th percentile, during the winter periods, which corresponds to the major storm events that occurred during the survey period (Figure 10a), *i.e.*, February 28, 2014 (6.23 m) during the Andrea storm, February 8, 2016 (6.81 m) during the Imogen storm, January 3, 2018 (6.07 m) during the Eleanor storm, and December 9, 2019 (6.10 m) during the Atiyah storm. Taking into account a significant wave height of >5 m, sixteen extreme events were inventoried from December 2012 to December 2019 (Table 1). The early spring period was also affected by extreme significant wave heights, as was the case during the Doris storm on March 9, 2016 (5.44 m).

Regarding the wave energy flux, a threshold up to 1.5 x 10^6 J/m² was defined taking into account a wave height of H_{m0} >5 m (99.9th percentile), associated with a period of 11.5 s, to describe the strongest events. Six storm events were inventoried, including Ruth on February 8-9, 2014, Andréa on February 28, 2014, the storm of February 24, 2015, Imogen on February 8, 2016, Eleanor on January 3, 2018, and Atiyah on December 9, 2019 (Table 1). Storm Imogen was the most significant event with more than 3.34 x 10^6 J.m^{-2} of energy (Figure 10b).

The major storm events inventoried using shallow wave height records are quite different from the ones related to offshore wave heights (Table 2). These events are well identified regarding shallow wave height (*i.e.*, Cristine, 2015-02-24, Eleanor, and 2019-12-13, storm events). Two more storm events were detected, *i.e.*, the low pressure system "Nadja" (2014-02-01), and Egon (2017-01-12/13). The absence of the Imogen storm is due to the fact that the OSSI pressure sensor did not record any data during this period (Figure 10c).

Significant major morphogenetic events combining highest storm waves and extreme water levels were statistically identified using a 3% exceedance threshold for observed tide and significant wave height (Figure 10d). Following this approach, seven significant morphogenetic events leading to a catastrophic overwash were detected. The major one exceeding 1% exceedance occurred January 3, 2018; it was related to storm Eleanor (Table 3).

4.3. Wave runup parameterisation

The wave runup parametrization is based on the simple equation from Hunt (1959) describing the linear relationship between the normalized wave runup and the beach slope divided by the offshore wave steepness, named by Battjes, 1974, the surf similarity parameter *Iribarren number* (ξ_0). This relationship can be written as follow:

$$\frac{R}{H_0} = C\xi_0 \qquad [3]$$

where C is a nondimensional constant, and ξ_0 is the Iribarren number given by:

$$\xi_0 = \frac{tan\beta}{\sqrt{H_0/L_0}} \qquad [4]$$

where tanβ is the beach slope, H_0 corresponds to offshore wave height (equivalent to H_{m0} for WW3-wave in deep water), and L_0 is the deep water wavelength using linear wave theory:

$$L_0 = \frac{gT_{m0,-1}^2}{2\pi} = 1{,}561T^2 \quad [5]$$

where g is the acceleration due to gravity; $T_{m0,-1}$ is the mean period; $2\pi/T$ is the radian frequency.

The dependence of wave runup on offshore and shallow wave parameters was assessed through a correlation analysis. Several parameters such as H_{m0} and $T_{m0,-1}$ for WW3 offshore deep water wave height, and the ratio of wave height to wave steepness $H_{m0}/(H_{m0}/L_0)^{0.5} = (H_{m0}L_0)^{0.5}$ were tested. As indicated by Poate et al. (2016) and Dodet et al. (2018), the importance of wave periods is better investigated using mean periods (*i.e.*, $T_{m0,-1}$), instead of peak period parameter (T_p).

For H_{m0} the square correlation (R^2) ranged respectively between 0.35 (profile A) and 0.41 (profile B) (Figure 11a). Considering the wave period ($T_{m0,-1}$) for the wavelength (L_0) calculation, Hunt (1959) indicates that both wave height and wave period are significant factors in determining the runup, and their combination in a Hunt-like parameter $(H_{m0}L_0)^{0.5}$ gives better fits. The square correlation increases to 0.49 and 0.50 (Figure 11b). Finally, the morphological component was considered by introducing the beach slope tanβ in the wave runup dependence on slope analysis. The correlation between R_{max} and tanβ $(H_{m0}L_0)^{0.5}$ once again increases to 0.54 and 0.55 (Figure 11c).

Based on this analysis, a parameterisation for the prediction of maximum runup (R_{max}) on the Sillon de Talbert was produced. The resulting optimised runup formula based on the offshore wave data set (WW3 wave parameters) is given by:

$$R_{max} = 0.58H_{m0}\xi_0 \text{ (for Profile A)} \quad [6]$$

$$R_{max} = 0.52H_{m0}\xi_0 \text{ (for Profile B)} \quad [7]$$

giving:

$$R_{max} = 0.5H_{m0}\xi_0 \text{ (for both profiles)} \quad [8]$$

4.4. Application of Orford and Carter's storm impact scale model

As indicated in the introduction, the storm impact scale model of Orford and Carter (1982) is based on the elevation difference between the extreme water level (EWL) –as the *peak overflow elevation (O_e)*–, and the height of the barrier crest (B_h). In this study, the EWL was calculated using equation [1], where the wave runup component was estimated using equations [6] and [7].

The height of the EWL was then subtracted from the height of the crest of the barrier (B_h) along both profiles in order to identify periods when the barrier was overtopped or discretely or severely overwashed (Figure 12). The flow depth ($O_{d,q}$) overtopping the crest barrier (see Orford and Anthony, 2011) was empirically thresholded by taking into account the morphological response of the barrier measured in the field to define three regimes corresponding to Orford and Carter's model. It appears that the overtopping regime takes place with O_d values between 0 and 25 cm, the discrete overwash regime with O_d values from 25 to 45 cm, and the overwash regime with O_d values greater than 45 cm (Figure 12b and 12e). The

catastrophic inundation regime was not retained because no breach openings were observed along the two measured profiles during the entire observation period. Moreover, the wave energy flux was calculated for each flow depth that overtopped/overwashed the barrier, and was plotted using proportional circles in order to identify the most morphogenic episodes (Figure 12b and 12e). In a way, the wave energy flux component can replace the volume (q) of the flow depth ($O_{d,q}$) and allows one to hierarchize the overtopping events according to the power of the flow. Finally, all these data were compared to the sediment budget calculated on the three sections of the barrier along the two profiles (see methodological section): the beach face, the crest, and the back of the barrier (Figure 12c and 12f).

The results show a strong similarity for both profiles. Three periods characterized by significant morphogenic events are inventoried. They show flow depth ($O_{d,q}$) levels of around >45 cm, inducing a sluicing overwash regime, notably *(i)* during the winter of 2013-2014 (January 3-4 with maximum $O_{d,q}$ of about 0.6 m for profile A, and 0.5 m for profile B; February 1-2 with maximum $O_{d,q}$ of about 0.8 m for profile A, and 0.5 for profile B; and March 3, 2014 with maximum $O_{d,q}$ of about 0.8 m for profile B, and 0.43 m for profile A), and *(ii)* during the Eleanor storm of January 3, 2018 with $O_{d,q}$ of about 0.7 m for profile A, and 0.43 for profile B. During the third event of February 9, 2016, corresponding to storm Imogen, the maximum $O_{d,q}$ reached about 0.7 m for profile B while the flow depth was much lower on profile A, reaching 0.36 m (Figure 12b and 12e).

In most cases, these sluicing overwash events generated the largest sediment transfers between the beach face and back barrier (Table 4). In some cases, the volumes removed from the beach face and the back-barrier perfectly balance (*e.g.*, 2014 February, 13 for both profiles), illustrating the rollover processes described and quantified by Suanez et al. (2018a). For cases where these volumes do not balance, notably when the volumes eroded at the beach face are less or greater than those accumulated at the back-barrier, we hypothesize that longshore sediment transfers have occurred in addition to the cross-shore sediment transfers due to rollover. These longshore sediment transfers have also been described and quantified by Suanez et al. (2020).

However, the wave energy flux (*i.e.*, F parameter) is involved in the change of the morphodynamic regime based on the flow depth ($O_{d,q}$). Indeed, for some events, the morphological response of the barrier spit generated by lower overtopping levels corresponding to the discrete overwash regime ($0.25<O_d<0.45$ m), was similar to that corresponding to a sluicing overwash regime with O_d >0.45 m. For example, this is the case for the Imogen storm of February 9, 2016 at profile A ($O_{d,q}$ of about 0.36 m), and the Eleanor storm of January 3, 2018 at profile B ($O_{d,q}$ of about 0.43 m) (Table 4 and Figure 12). Therefore, the wave energy flux (*i.e.*, F parameter) indicates that the application of the Orford and Carter's storm impact scale model might be improved by considering this component.

5. Discussion

5.1. Barrier migration rates

The Sillon de Talbert experienced a significant landward migration during the survey period (2012-2019), with maximum values reaching –23 to –30 m for profiles A and B respectively, corresponding to –3.3 to –4.3 m.y^{-1}. By comparison, the pluri-secular landward migration rates (1775-1966) estimated by Pinot (1994) reached about –0.5 m.y^{-1}. For the last several decades (1930-2010), Stéphan et al. (2012) calculated a maximum retreat reaching about –1.6 m.y^{-1}, increasing to between –3.5 to –4 m.y^{-1} from 2002 to 2017 (Stéphan et al., 2018; Suanez et al., 2018a).

The acceleration of the rate of landward migration for the Sillon de Talbert spit during the past decades raises the question of the SLR implication. The long-term analysis of SLR based on a dataset recorded at Roscoff station (see Figure 2a) indicates a sea-level rise reaching of 1.8 □0.26 mm.yr^{-1} and 1.23 □0.6 mm.yr^{-1} over both periods 1970-2018 and 1993-2018 (Dodet et al., 2019). Therefore, there is no evidence of an increase in SLR over the last 25 years. For the Sillon de Talbert, Orford et al. (1995b) estimated the migration rate to about 0.32 m.yr^{1} expected with a SLR rate of 1 mm.yr^{-1}. According to the SLR estimated by Dodet et al. (2019), the landward migration of the Sillon de Talbert would have reached –28 m over the period of 1970-2018 to –10 m over the period of 1993-2018. These values are far below the measurement of the barrier landward retreat performed by Stéphan et al. (2012). In addition, the analysis of extreme water level (EWL) (including predicted tide + surge + wave runup) conducted by Stéphan et al. (2012) over the period of 1979-2010, showed no evidence of an increase in significant morphogenetic events leading to barrier overwash processes. Therefore, meso to macroscale (>10^1 to 10^2 yr) SLR cannot adequately explain the increase of landward migration rates of the Sillon de Talbert barrier spit, at least since the early 2000s. According to the results obtained in this study, about 83% to 90% (respectively for profile A and B) of the global retreat of the Sillon de Talbert is related to the impact of three significant morphogenic episodes combining energetic storm waves and high spring tide levels (*i.e.*, February 1-2 2014, the Imogen storm of February 9 2016, and the Eleanor storm of January 3-4 2018), with a frequency of occurrence of 2 to 3 years. If we extend the analysis to the early 2000s (see Suanez et al., 2018a), a few additional episodes with a frequency of occurrence of 2 to 4 years, including the storm of March 10, 2008, can also be considered. These results are in agreement with those obtained by Orford et al. (1995a, 1995b) and confirm the determining role of microscale (<10^0 yr) SLR. The increase in the frequency of occurrence of significant morphogenetic events (i.e. combining storm and high spring tide) could be related to a change in the regime of high winter wave heights (decile 90th) in the northern part of the North-East Atlantic (Dodet et al., 2010). The long-term analysis (1953-2009) conducted by the authors shows an increasing trend up to 1.2 m (0.02 m.yr^{-1}) of winter-means (from 1st of December to 1st of April) H_{s90} at 55°N of latitudes. Thus, increasing storm magnitude also increases the likelihood of EWL inducing barrier overwash when combined with high tide levels.

The increase of barrier landward migration over the last several decades has also been reported by Forbes et al. (1991) on the Story Head barrier (Atlantic coast of Nova Scotia). The authors indicated a landward migration rate of about –1 m.yr^{-1} between 1854 to 1917, –2 m.yr^{-1} between 1917 and 1954, and –6 to –8 m.yr^{-1} between 1954 and 1988. Regarding the same dataset, Orford et al. (1991) analyzed the link between the sea-level change and the retreat of the barrier by distinguishing both the landward migration of the beach face and the back-barrier. They indicated that the landward migration of the seaward barrier shoreline was linearly proportional to the mesoscale (10^0 to 10^2 yr) sea-level change, however the back-barrier migration rate is not significantly related to these rates of sea-level change. The authors interpreted this difference between seaward and back-barrier migration as the role of storm intensity (frequency and magnitude) superimposed on long-term sea-level change. Orford et al. (1995a) indicated that barrier retreat best fit with the sub-decadal (<10^1 yr) SLR rate which

controls surge frequency/magnitude, recognized as the dynamic landward migration through crest overwashing processes. The authors concluded that mesoscale (10^0-10^2 yr) rather than macroscale (>10^2 yr) SLR rate is the critical control on barrier retreat, as mesoscale SLR variations in combination with surge potential are able to raise water level to the elevation threshold sufficient for barrier overwash and hence drive barrier retreat. They specifically noted that the higher the sub-decadal sea-level rise rate, the faster the rate of retreat of the swash-aligned gravel barrier (Orford et al., 1995b).

However, the relationship between mesoscale sub-decadal SLR and barrier retreat is also a function of the barrier's inertia as defined by the barrier's cross-sectional volume (Orford et al., 1995b, 2002). The authors concluded that the smaller the barrier's cross sectional area, the faster the retreat rate regardless of the decadal-mesoscale rate of SLR. The cross-sectional volumes of the profiles A and B are 287 and 348 m^3, respectively, while the barrier retreat reaches –23 m for profile A and up to –30 m for profile B over the survey period (2012-2019). From these observations, we can see that Orford et al. (1995b), barrier inertia "model" does not seem to work in our case.

In addition, the evolution of these volumes for both profiles between 2002 and 2019 shows a decrease in the sediment budget for profile A (about –35 m^3), while profile B gained about +50 m^3 of sediment (Figure 13). This evolution supports the trend of the global sediment budget of the spit for the last 15 years (Stéphan et al., 2018; Suanez et al., 2018a). Profile A, located closest to the proximal part of the spit, loses more sediment than profile B located further NE towards the distal part. This contrast illustrates the cannibalization phenomenon from which the sediments eroded at the proximal part feed the distal part of the spit due to the sediment transfer generated by the longshore drift oriented SW-NE.

Similarly, the sediment budget calculated over the survey period (2012-2019) also indicates a difference in evolution between the two profiles. Profile B shows a significant increase of about +27 m^3.m.l., while the gain recorded by profile A is much lower (+11 m^3.m.l.). These data also confirm that the Orford et al. (1995b), barrier inertia "model" does not work in this case.

The sediment grain size distribution of the upper part of the barrier, including the crest, must then be taken into account to explain the differences in migration speed between the two profiles, and the fact that Orford et al. (1995b) model does not work in this case. The high proportion of sand inside the barrier body along the profile A (see above, section 3.1.) fills the interstitial voids, increasing the inertia of the barrier because the coarser sediments (i.e., gravel fraction) are trapped in the sandy matrix. The rollover process inducing the landward barrier migration is therefore diminished because the coarse sediments are less mobile. Conversely, the high proportion of coarser sediments (i.e., gravels) on the profile B favors the gradual accumulation of coarse material on the crest through overstopping resulting in steeper beachface gradients (Masselink and Li, 2001). The greater the volumes of sediment accumulated on the crest, the greater the landward displacement by rollover during catastrophic overwash event. Thus, in the case of the profile A, the high proportion of sandy sediments inhibits overtopping processes and reduces the potential overwashed volumes of sediments (and thus, the speed retreat of the barrier).

The remaining 10% to 17% of barrier spit retreat corresponds to processes of adjustment of the slope of the back barrier slope, notably during phases of morphogenic calm. During these phases of fair weather conditions, the crest of the barrier rises under the action of small fair-weather waves, while the slope of the front beach steepens (Figure 9). At the same time, the slope of the back-barrier decreases due to equilibrium slope readjustment processes. These

processes are particularly illustrative of the rollover phenomenon described by Orford and Anthony (2011).

5.3. Calibration of runup formula

According to Stockdon et al. (2006), who analyzed a large runup dataset acquired on several sandy beaches, the highest wave runup ($R_{2\%}$) is dominated by energetic incident wave for reflective conditions associated to plunging and collapsing/surging breakers as indicated by Iribarren number (ξ_0>1.25). In our case, both profiles show rather intermediate to reflective morphodynamic conditions with an average Iribarren number (ξ_0) between 0.83 (with max up to 2.66) and 1.28 (with max up to 4.27) for profiles A and B, respectively. The authors distinguished the $R_{2\%}$ runup elevation between incident and infragravity frequencies and showed that the dimensional incident swash better fit with $\xi_0 H_0 = \tan\beta\ (H_0 L_0)^{1/2}$ for reflective conditions, while the dimensional infragravity swash better scaled with $(H_0 L_0)^{1/2}$. Following the same approach, we demonstrated that taking into account the beach slope through the Irribaren number (ξ_0) substantially improved the mathematical model from 49-50% R^2 significance for $(H_0 L_0)^{1/2}$ to 54-55% for $\tan\beta\ (H_0 L_0)^{1/2}$ (Figure 11). Stockdon et al. (2006) proposed the following simplified expression for runup for reflective conditions with an rms error of 47 cm:

$$R_{2\%} = 0.73\beta_f\ (H_0 L_0)^{1/2} \qquad [9]$$

where β_f is beach slope.

The use of Stockdon's equation (which is one of the most widely used runup predictors at present) shows that the results obtained for the two profiles overestimate the field reality by about 0.5 m for profile A, and by more than 0.7 m for profile B (Figure 14), even though Stockdon's equation is calibrated for a runup of 2% exceedance ($R_{2\%}$), while our is for a maximum runup (R_{max}). While for profile A, this overestimation is within the orders of magnitude of the rms reported by Stockdon et al. (2006), it is much larger for profile B.

The overestimation of the Stockdon's equation can be explained by the fact that it has been calibrated on sandy beaches, which have moderate roughness and porosity compared to gravel environments. In our case, the largest bed roughness for gravel particles induces a flow retardation, which may also be increased by higher the percolation leading to a loss of swash volume. Both processes contribute to limit the runup, explaining that the porous structures are widely used as breakwaters for coastal defence (Twu and Chieu, 2000; Venkateswarlu and Karmakar, 2019; Guo et al., 2020). In addition, as indicated by Poate et al. (2016), while these equations fit the range of gravel beach field data, the inclusion of a dimensional constant (C) implies that the equations can only be used for conditions similar to those in the field and model data set. That makes difficult to transpose an equation calibrated on one specific site to another one.

The barrier dynamics are thus strongly affected by the gravel dynamics, including coarse particle size and strong percolation of water inside the porous media, leading to enhanced wave dissipation. Applying Xbeach-G in several environments, including our study site, McCall et al. (2015) demonstrated the difficulty in reproducing the morphodynamic response of the Sillon de Talbert during the Johanna storm of March, 10 2008. The Xbeach-G simulations predicted higher wave dissipation than observed, likely caused by higher estimates of overwash. The new dataset presented here, with a precise distribution of grain size over the

whole profile, could help future studies considering the influence of the granulometry distribution in Xbeach-G. Grain size plays a major role in this environment, impacting the wave dissipation, backwash and overwash gravel transport and cascading effects.

5.4. Validation of the Orford and Carter's storm impact scale model

Based on the morphological changes, especially of the crest and the back-barrier, an empirical thresholding of the overtopping levels was proposed to distinguish the different regimes of Orford and Carter's storm impact scale model (Orford and Carter, 1982). Thus, the overtopping regime was defined as between 0 and 0.25 m, the discrete overwash regime between more than 0.25 and 0.45 m, and the overwash regime greater than 0.45 m, while the catastrophic inundation regime was not retained because no breach openings were observed along the two measured profiles over the entire observation period. These levels of overtopping are particularly indicative of the major significant morphogenic events that generated a landward retreat of the barrier. In our case, it is the three events of February 1-2, 2014, February 9, 2016, and January 3, 2018. This landward migration is also very well indicated by changes in the sediment budget, particularly between the front and back beaches. In general, we can attest that Orford and Carter's model works well, and that it allows one to model the most noteworthy morphogenic episodes contributing to significant morphological changes of the barrier beach, including the landward retreat by the rollover process.

The results obtained in this study show, however, that wave energy flux is a key factor in the change of morphodynamic regime, for instance from discrete to sluicing overwash. Thus, this energetic parameter constitutes a third variable in addition to the observed tide (including the surge) and the wave runup in the quantification of the hydrodynamic forcing ($O_{d,q}$) of Orford and Carter's model. Therefore, the flow depth ($O_{d,q}$) component proposed by Orford and Anthony (2011), where d is the depth, and q the volume of the flow, could be redefined as ($O_{d,F}$), considering the wave energy flux parameter (F) is first, much easier to calculate than the volume (q) of water overtopping the barrier. Secondly, considering the same extreme water level O_e for the following two cases *(i)* high spring tide + low surge + low wave condition (inducing a low runup), *(ii)* small spring tide + large surge + high wave condition (inducing a high runup), the morphological changes will be more significant in the second case because the wave energy flux is proportionally higher.

Conclusion

The high-frequency topomorphological and hydrological survey of the Sillon de Talbert underway since September 2002, has definitely enhanced the understanding of the morphodynamic functioning of this gravel spit. The main result of this survey is the calculation of the rapid landward migration rate, reaching –3.3 to –4.3 m.y^{-1} over the last 7 years (September 2012 to December 2019), which is of the same magnitude as the retreating rates measured over the last 20 years (2002-2021). These values indicate an eightfold increase in the speed of the landward migration of the spit since the 18th century, and a two- to threefold increase since the beginning of the 20th century. This rapid retreat is not related to long-term sea level rise (*i.e.*, macroscale of 10^2 to 10^3 yr forcing), but to the impact of short-term morphogenic events (*i.e.*, micro to mesoscale of 10^0 to10^2 yr processes) combining storm waves and high spring tides. These short-term processes are fairly well quantified and modeled from the storm-impact scale model of Orford and Carter (1982). Over 83% to 90% of the barrier spit retreating occurs under the sluicing overwash regime and/or by discrete overwash when the wave energy flux is sufficient to generate catastrophic overwash conditions. The remaining

10% to 17% corresponds to processes of adjustment of the equilibrium slope of the back barrier, notably during phases of morphogenic calm.

References

Battjes J.A. 1974. *Surf similarity.* Proceedings of the 14th International Conference on Coastal Engineering ASCE, Copenhagen (Denmark), 24-28 June 1974: 466–480.

Barnard P., Hoover D., Hubbard D., Snyder A., Ludka B.C., Allan J., Kaminsky G.M., Ruggiero P., Gallien T.W., Gabel L., McCandless D., Weiner H.M., Cohn N., Anderson D.L., Serafin K.A. (2017) - Extreme oceanographic forcing and coastal response due to the 2015–2016 El Niño. *Nature Communications* **8,** 14365.

Bishop C.T., Donelan M.A. 1987. Measuring waves with pressure transducers. *Coastal Engineering* **11**(4): 309-328.

Blaise E., Suanez S., Stéphan P., Fichaut F., David L., Cuq V., Autret R., Houron J., Rouan M., Floc'h F., Ardhuin F., Cancouët R., Davidson R., Costa S., Delacourt C. 2015. Bilan des tempêtes de l'hiver 2013-2014 sur la dynamique de recul du trait de côte en Bretagne. *Géomorphologie : Relief, Processus, Environnement* **21**(3): 267–292.

Boudière E., Maisondieu C., Ardhuin F., Accensi M., Pineau-Guillou L., Jérémy Lepesqueur J. 2013. A suitable metocean hindcast database for the design of Marine energy converters. *International Journal of Marine Energy* **3-4**: e40–e52.

Brown S.I., Dickson M.E., Kench P.S., Bergillos R.J. 2019. Modelling gravel barrier response to storms and sudden relative sea-level change using XBeach-G. *Marine Geology* **410**: 164–175.

Cariolet J.-M., Suanez S. 2013. Runup estimations on macrotidal sandy beach. *Coastal Engineering* **74**: 11–18.

Carter R.W.G., Orford J.D. 1993. The morphodynamics of coarse clastic beaches and barriers: a short and long-term perspective. *Journal of Coastal Research* **15**(SI): 158–179.

Didier D., Caulet C., Bandet M., Bernatchez P., Dumont D., Augereau E., Floc'h F., Delacourt C. 2020. Wave runup parameterization for sandy, gravel and platform beaches in a fetch-limited, large estuarine system. *Continental Shelf Research* **192**: 104024.

Davies J.L. 1972. Geographical variation in coastal development, Oliver and Boyd, Edinburgh.

Dodet G., Bertin X., Taborda R. 2010. Wave climate variability in the North-East Atlantic Ocean over the last six decades. *Ocean Modelling* **31**: 120-131.

Dodet G., Leckler F., Sous D. Ardhuin F., Filipot J.-F., Suanez S. 2018. Wave runup over steep rocky cliffs. *Journal of Geophysical Research: Oceans* **123**(10): 7185-7205.

Dodet G., Bertin X., Bouchette F., Gravelle M., Testut L., Wöppelmann G. 2019. Characterization of sea-level variations along the metropolitan coasts of France: Waves, tides, storm surges and long-term changes. *Journal of Coastal Research,* **88**(SI): 10–24.

Fichaut B., Martin N., Stéphan P., Suanez S. 2015. Caractérisation de la sédimentologie du Sillon du Talbert (Commune de Pleubian – Juillet 2014). Rapport d'expertise (mars 2015), LETG-UMR 6554 CNRS, 23p. https://hal.archives-ouvertes.fr/hal-01141243/document

Forbes D.L., Taylor R.B., Orford J.D., Carter R. W. G., Shaw J. 1991. Gravel-barrier migration and overstepping. *Marine Geology* **97**(3–4): 305–313.

Grieco M.B., DeGaetano A.T. 2019. A climatology of extreme wave height events impacting eastern Lake Ontario shorelines. *Theoretical and Applied Climatology* **136**: 543–552.

Guo Y.C., Mohapatra S.C., Soare C.G. 2020. Wave energy dissipation of a submerged horizontal flexible porous membrane under oblique wave interaction. *Applied Ocean Research* **94**, 101948.

Homma M., Horikawa K., Komori S. 1966. Response characteristics of underwater wave gauge. *Coastal Engineering in Japan* **9**(1): 45-54.

Hunt I.A. 1959. Design of seawalls and breakwaters. *Journal of the Waterways and Harbors Division.* **85**(3): 123–152.

IAHR (the) Working Group on Wave Generation and Analysis. 1989. List of sea-state parameters. *Journal of Waterway, Port, Coastal, and Ocean Engineering* **115**(6): 793-808.

Lamb H.H., Frydendahl K. 2005. Historic storms of the North Sea, British Isles and Northwest Europe, Cambridge University Press, Cambridge.

Lazure P., Dumas F. 2008. An external-internal mode coupling for a 3D hydrodynamical model for applications at regional scale (MARS). *Advances in Water Resources* **31**: 233–250.

Masselink G., Li L. 2001. The role of swash infiltration in determining the beachface gradient: a numerical study. *Marine Geology* **176**: 139–156.

Masselink G., van Heteren S. 2014. Response of wave-dominated and mixed-energy barriers to storms. *Marine Geology* **352**: 321–347.

Matias A., Williams J.J., Masselink G., Ferreira Ó. 2012. Overwash threshold for gravel barriers. *Coastal Engineering* **63**: 48–61.

McCall R.T., Masselink G., Poate T.G., Roelvink J.A., Almeida L.P. 2015. Modelling the morphodynamics of gravel beaches during storms with XBeach-G. *Coastal Engineering* **103**, 52-66.

Morel V. 1998. De la géomorphologie à la gestion des cordons de galets littoraux du bassin de la Manche et de ses abords : études de cas (Bretagne, Haute-Normandie, Picardie, Sud Angleterre) et réflexions générales. PhD Thesis, Université de Bretagne Occidentale, 386p.

Orford J.D., Carter R.W.G. 1982. Crestal overtop and washover sedimentation on a fringing sandy gravel barrier coast, Carnsore Point, Southeast Ireland. *Journal of Sedimentary Research* **52**(1): 265–278.

Orford J.D., Carter R.W.G., Forbes D.L. 1991. Gravel barrier migration and sea level rise: some observations from Story Head, Nova Scotia, Canada. *Journal of Coastal Research* **7**(2): 477–488.

Orford J.D., Carter, R.W.G. Jennings S.C., Hinton A.C. 1995a. Processes and timescales by which a coastal gravel-dominated barrier responds geomorphologically to sea-level rise: Story head barrier, Nova Scotia. *Earth Surface Processes and Landforms* **20**(1): 21–37.

Orford J.D., Carter R.W.G., McKenna J., Jennings S.C. 1995b. The relationship between the rate of mesoscale sea-level rise and the rate of retreat of swash-aligned gravel-dominated barriers. *Marine Geology* **124**(1–4): 177–186.

Orford J.D., Carter R.W.G. 1995. Examination of mesoscale forcing of a swash-aligned, gravel barrier from Nova Scotia. *Marine Geology* **126**(1–4): 201–211.

Orford J.D., Carter R.W.G., Jennings S.C. 1996. Control domains and morphological phases in gravel-dominated coastal barriers of Nova Scotia. *Journal of Coastal Research* **12**(3): 51–85.

Orford J.D., Forbes D.L., Jennings S.C. 2002. Organisational controls, typologies and time scales of paraglacial gravel-dominated coastal systems. *Geomorphology* **48**(1–3): 51–85.

Orford J.D., Anthony E.J. 2011. Extreme events and the morphodynamics of gravel-dominated coastal barriers: strengthening uncertain ground. *Marine Geology* **290**: 41-45.

Phillips B.T., Brown J.M., Plater A.J. 2020. Modeling impact of intertidal foreshore evolution on gravel barrier erosion and wave runup with XBeach-X. *Journal of Marine Science and Engineering* **8**(11): 914.

Pierson W.J., Marks W. 1952. The power spectrum analysis of ocean-wave records. *Eos, Transactions American Geophysical Union* **33**(6): 834–844.

Pinot J-P. 1994. Fixer le plan ou gérer le profil : l'exemple du Sillon du Talbert. *Cahiers Nantais* **41-42**: 307–316.

Plant N.G., Stockdon H.F., 2015. How well can wave runup be predicted? Comment on Laudier et al. (2011) and Stockdon et al. (2006). *Coastal Engineering* **102**: 44–48.

Poate T.G., McCall R.T., Masselink G. 2016. A new parameterisation for runup on gravel beaches. *Coastal Engineering* **117**: 176–190.

Polidoro A., Dornbusch U., Pullen T. 2013. Improved maximum run-up formula for mixed beaches based on field data. ICE Coasts, Marine Structures and Breakwaters Conference, Edinburgh, 389–398.

Pollard J.A., Christie E.K., Brooks S.M., Spencer T. 2021. Impact of management regime and regime change on gravel barrier response to a major storm surge. *Journal of Marine Science and Engineering* **9**(2): 147.

Powell K.A. 1990. Predicting short term profile response for shingle beaches. Hydraulics Research Limited, Wallingford, Oxfordshire. Report SR 219, 74p. + Tables, Figures, and Appendices. https://eprints.hrwallingford.com/263/1/SR219.pdf

Roland A., Ardhuin F. 2014. On the developments of spectral wave models: numerics and parameterizations for the coastal ocean. *Ocean Dynamics* **64:** 833–846,

Saha S., Moorthi S., Pan H.-L., Wu X., Wang J., Nadiga S., et al. 2010. The NCEP Climate Forecast System Reanalysis. *Bulletin of American Meteorology Society* **91:** 1015–1057.

SHOM. 2016. Références altimétriques maritimes – Ports de France métropolitaine et d'outre–mer. Côtes du zéro hydrographique et niveaux caractéristiques de la marée. Service Hydrographique et Océanographique de la Marine, Brest.

Stéphan P., Suanez S., Fichaut B. 2010. Franchissement et recul des cordons de galets par rollover. Impact de la tempête du 10 mars 2008 dans l'évolution récente du Sillon de Talbert (Côtes d'Armor, Bretagne). *Norois* **215**: 59–75.

Stéphan P., Suanez S., Fichaut B. 2012. Long-term morphodynamic evolution of the Sillon de Talbert gravel barrier (Brittany, France). *Shore & Beach* **80**(1): 19–36.

Stéphan P., Suanez S., Fichaut B., Autret R., Blaise E., Houron J., Ammann J., Grandjean P. 2018. Monitoring the medium-term retreat of a gravel spit barrier and management strategies, Sillon de Talbert (North Brittany, France). *Ocean & Coastal Management* **158**: 64–82.

Stockdon H.F., Holman R.A., Howd P.A., Sallenger A.H. 2006. Empirical parameterization of setup, swash, and runup. *Coastal Engineering* **53**: 573–588.

Suanez S., Cancouët R., Floc'h F., Blaise E., Ardhuin F., Filipot J.-F., Cariolet J.-M., Delacourt C. 2015. Observations and predictions of wave runup, extreme water levels, and medium-term dune erosion during storm conditions. *Journal of Marine Science and Engineering* **3**(3): 674–698.

Suanez S., Stéphan P., Floc'h F., Autret R., Fichaut B., Blaise E., Houron J., Ammann J., Grandjean P., Accensi M., André G., Ardhuin F. 2018a. Fifteen years of hydrodynamic forcing and morphological changes leading to breaching of a gravel spit, Sillon de Talbert (Brittany). *Géomorphologie : Relief, Processus, Environnement* **24**(4): 403–428.

Suanez S., Stéphan P., Houron J. 2018b. Données du suivi mensuel de profils de plage de la flèche de galets du Sillon de Talbert (Pleubian, Bretagne nord). INDIGEO. https://doi.org/10.35110/5000bf97-652e-4cef-863e-572d0cbceac3

Suanez S., Stéphan P., Floc'h F. 2018c. Mesures des conditions hydrodynamiques côtières le long du Sillon de Talbert (Pleubian, Bretagne nord). INDIGEO. https://doi.org/10.35110/f6f2440a-4703-4352-8f3e-3f3999472b3c

Suanez S., Stéphan P., Fichaut B., Ammann J., Accensi M. 2020. Medium-Term Longshore and Cross-shore Dynamics of a Gravel Spit Driving by Storm Events (Sillon de Talbert, Brittany, France). *Journal of Coastal Research* **95**(spl): 669–673.

Tolman H.L. (and the WAVEWATCH III® Development Group) (2014) - User Manual and System Documentation of WAVEWATCH III® version 4.18, Technical Note 316, NOAA/NWS/NCEP/MMAB, 282p. + Appendices.

Twu S.W., Chieu C.C. 2000. A highly wave dissipation offshore breakwater. *Ocean Engineering* **27**(3), 315-330.

Venkateswarlu V., Karmakar D. 2019. Numerical investigation on the wave dissipating performance due to multiple porous structures. *ISH Journal of Hydraulic Engineering* **27**(spl): 202-219.

H_{m0} >5 m (99.9% percentile)	Extreme events (storms)	Wave energy flux (F)
2013-02-05 6h (5.16 m)	*low pressure system « Pille »*	*
2014-02-09 5h (5.25 m)	Ruth	($1.57*10^6$ J/m²)
2014-02-28 9h (5.80 m)	Andrea	($1.79*10^6$ J/m²)
2015-01-29 19h (5.20 m)	*low pressure system « Mischka »*	*
2015-01-30 7h (5.59 m)	*low pressure system « Mischka »*	*
2016-02-08 10h (6.13 m)	Imogen	($2.11*10^6$ J/m²)
2016-03-02 14h (5.11 m)	*no name*	*
2016-03-09 11h (5.07 m)	*low pressure system « Doris »*	*
2016-03-09 19h (5.11 m)	*low pressure system « Doris »*	*
2016-03-09 21h (5.10 m)	*low pressure system « Doris »*	*
2018-01-03 9h (5.89 m)	Eleanor	($1.82*10^6$ J/m²)
2018-12-09 10h (5.33 m)	*no name*	*
2018-01-16 22h (6.19 m)	Fionn	($2.00*10^6$ J/m²)
2019-01-27 12h (5.00 m)	Martin	*
2019-12-09 6h (6.21 m)	Atiyah	($2.02*10^6$ J/m²)
2019-12-13 9h (5.79 m)	*no name*	($1.56*10^6$ J/m²)

Table 1

$H_{m0} \geq 1.8$ m	Storm event
2014-02-01 18h-20h (2.05 to 2.10 m)	*Low Pressure System "Nadja"*
2014-03-03 19h (2.12 m)	Christine
2015-02-24 9h (1.94 m)	*no name*
2017-01-13 6h (1.94 m)	Egon
2018-01-03 05h-07h (1.93 to 2.12 m)	Eleanor
2019-12-13 6h (1.93 m)	*no name*

Table 2

97% joint event	99% joint event
2014-02-01 6h55 – *no name* (tide: 6.18 m ; H_{m0} = 3.24 m)	
2014-02-01 19h23 – *no name* (tide: 5.53 m ; H_{m0}: 3.99 m)	
2014-02-02 7h41 – *no name* (tide: 5.88 m ; H_{m0}: 3.17 m)	
2016-02-09 6h24 - Imogen (tide: 5.98 m ; H_{m0}: 3.06 m)	
2016-03-09 6h06 – low pressure Doris (tide: 5.81 m ; H_{m0} = 3.15 m)	
2017-02-28 7h09 – *no name* (tide: 5.53 m ; H_{m0}: 3.07 m)	
2018-01-04 7h23 – Eleanor (tide: 5.70 m ; H_{m0}: 3.51 m)	2018-01-03 6h35 – Eleanor (tide: 5.80 m ; H_{m0}: 5.39 m)

Table 3

	Profile A			Profile B		
	beach face	crest barrier	back-barrier	beach face	crest barrier	back-barrier
07/01/2014	–17 □2	0	+30.5 □1.8	–7 □1.6	+5	0
13/02/2014	–39 □2	0	+34 □1.9	–99 □2	0	+97 □1.6
05/03/2014	-0.1 □2	+0.8 □1.3	+24.5 □1.2	–26 □2	0	+27 □1.3
12/02/2016	–1.2 □2	–2.4 □1.3	+17.3 □1.5	–15 □2	0	+31.5 □1.3
05/01/2018	–23 □2	0	+13.5 □1.7	–44 □2	0	+44 □1

Table 4

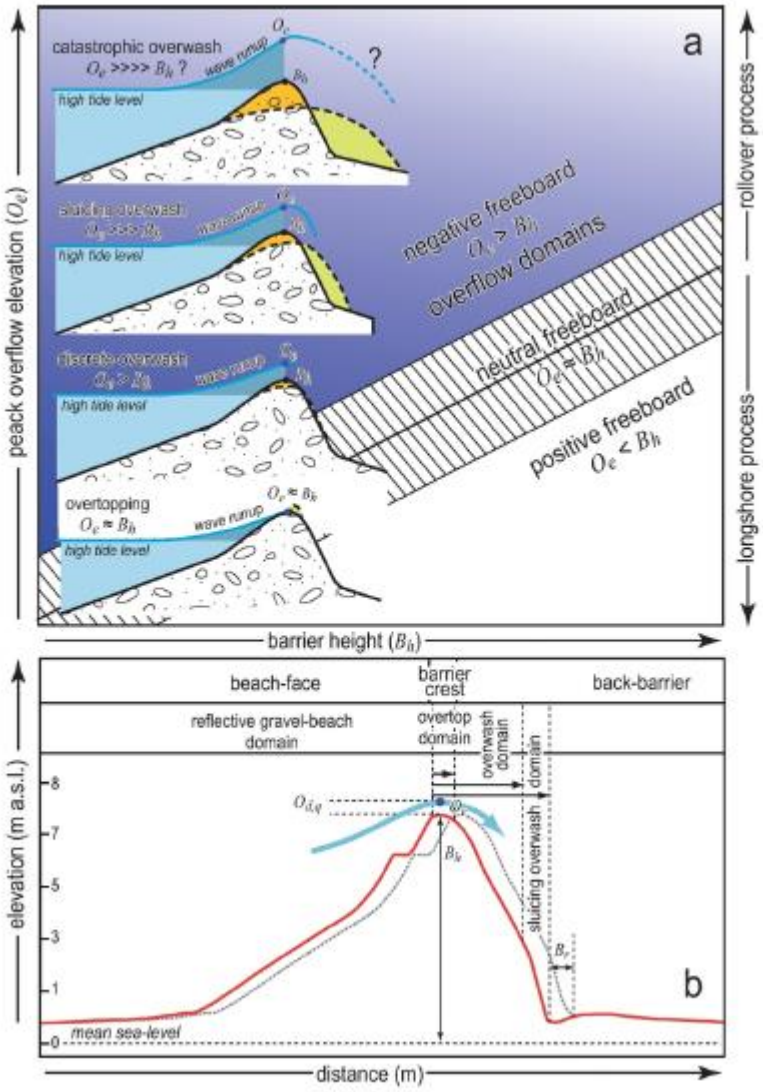

Figure_01

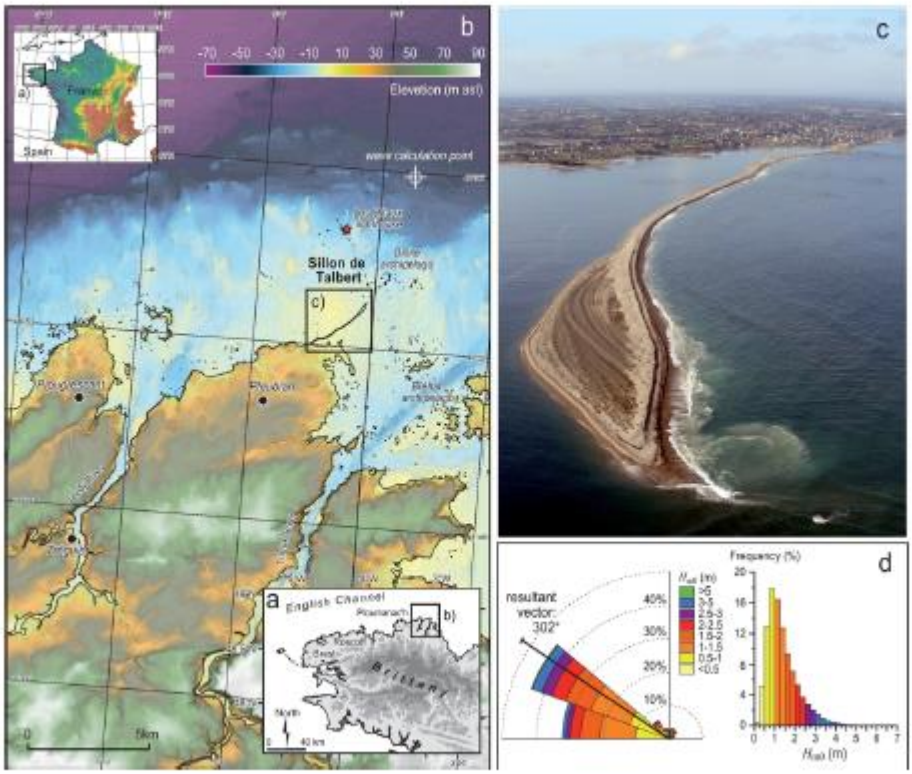

Figure_02

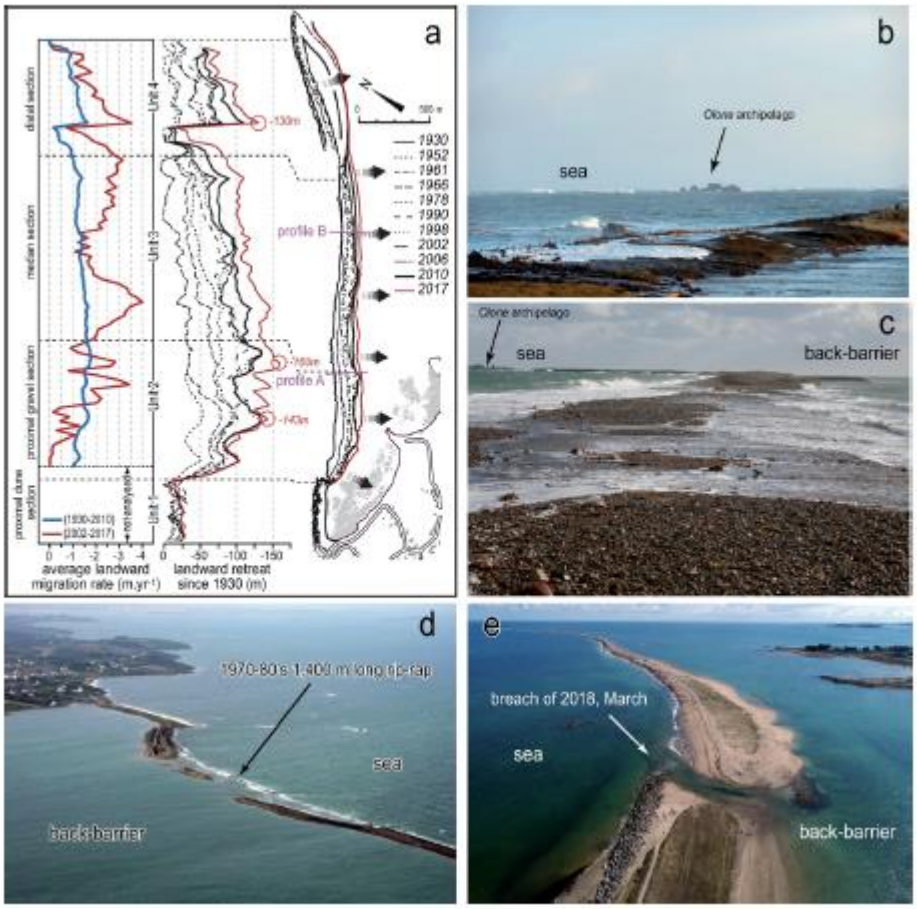

Figure 3

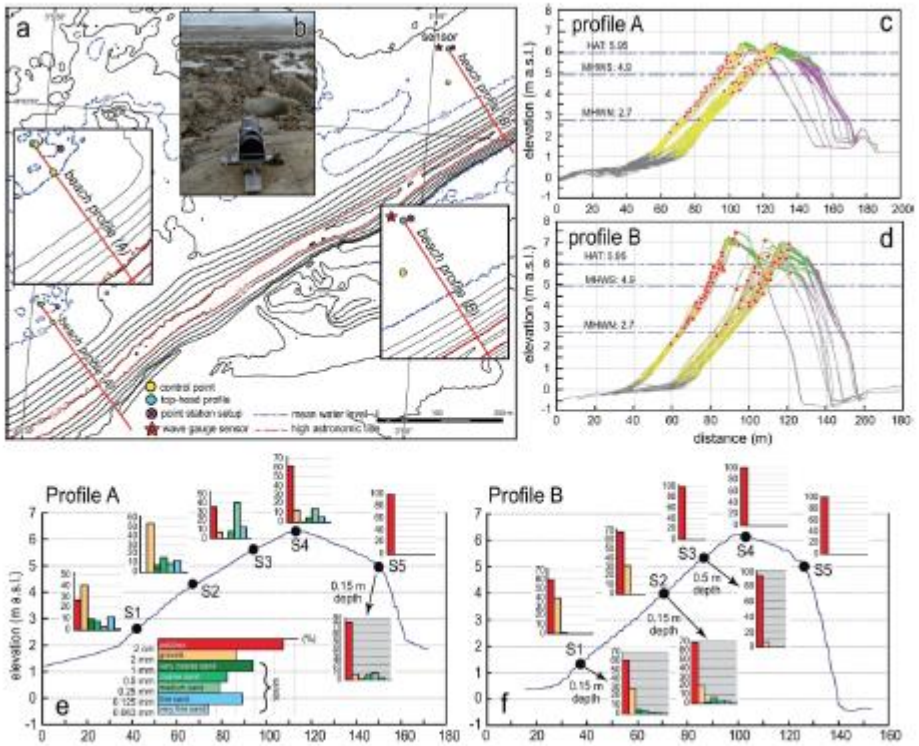

Figure_04

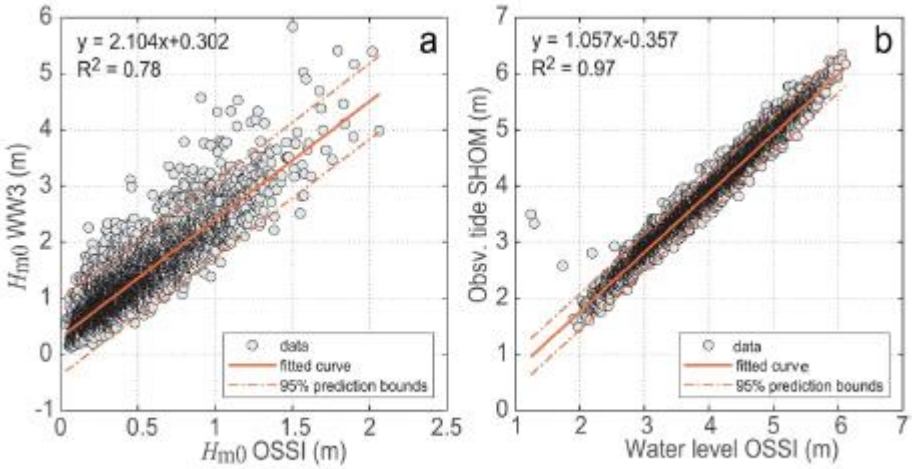

Figure_05

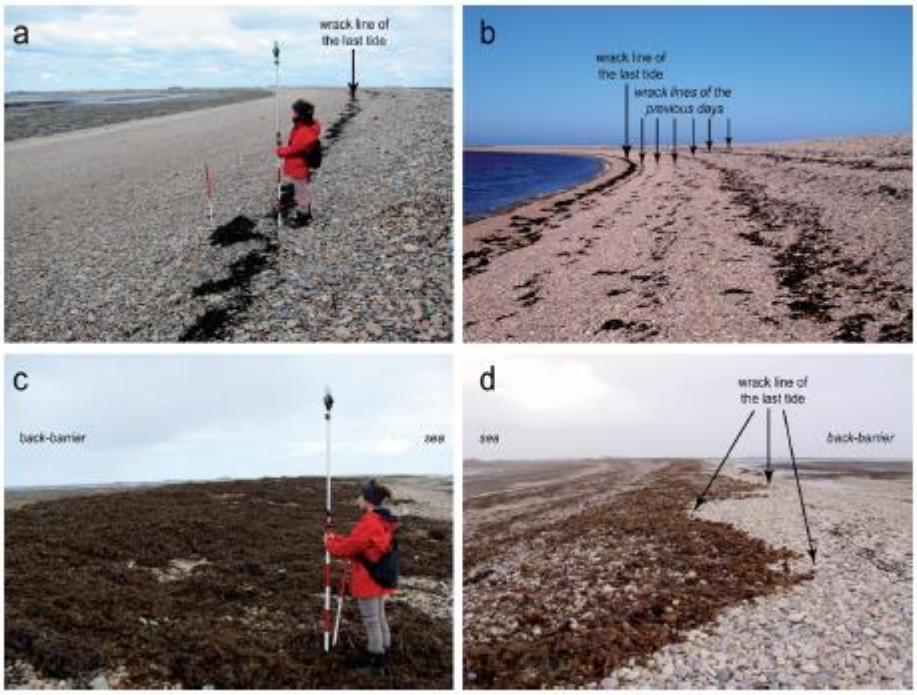

Figure_06

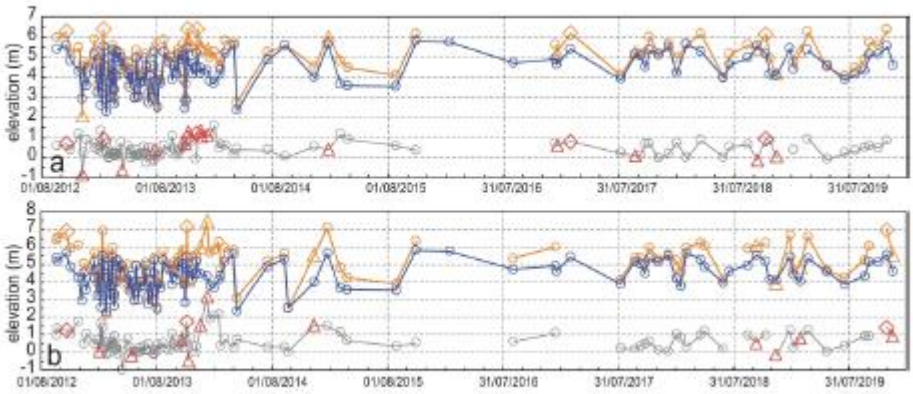

Figure_07

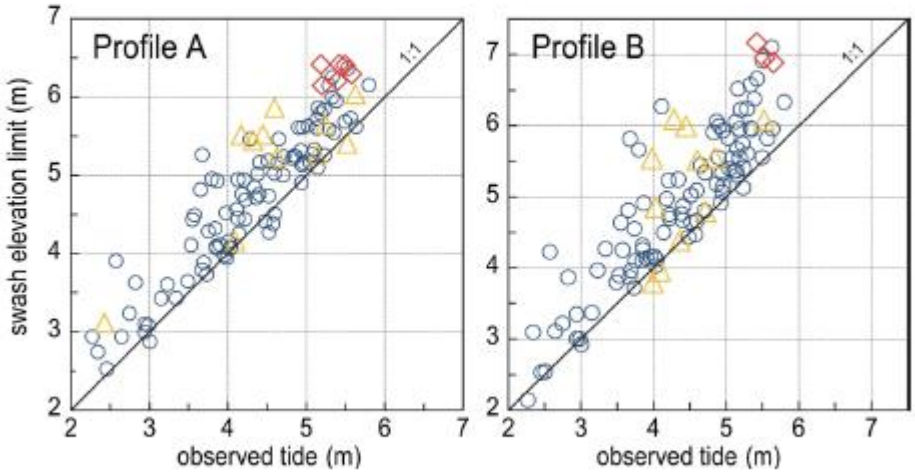

Figure_08

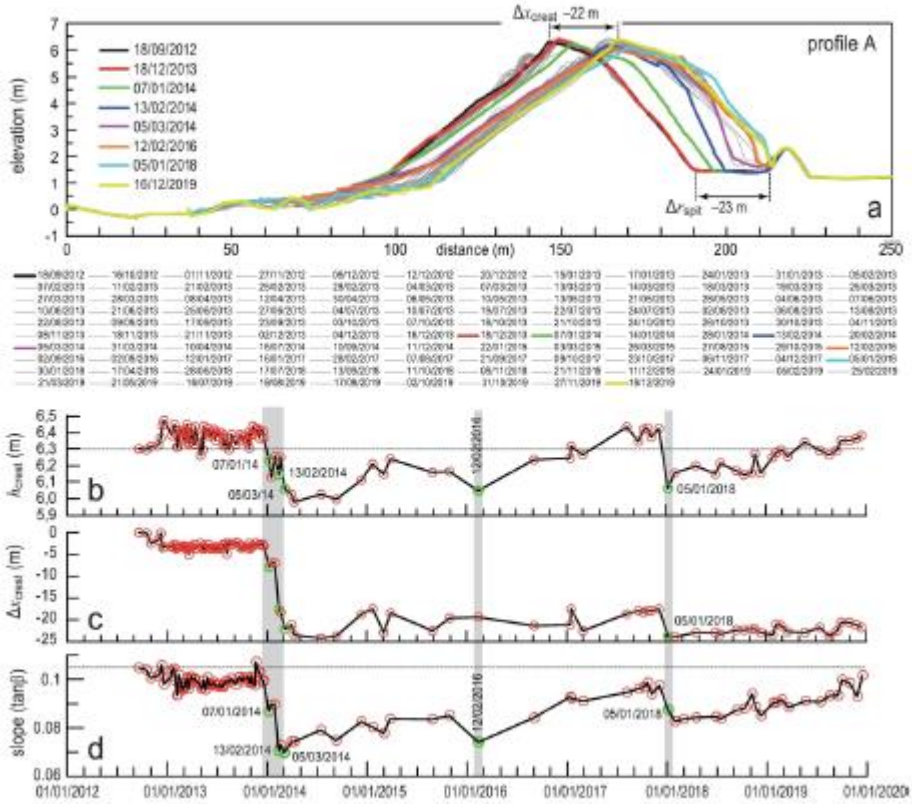

Figure_09a

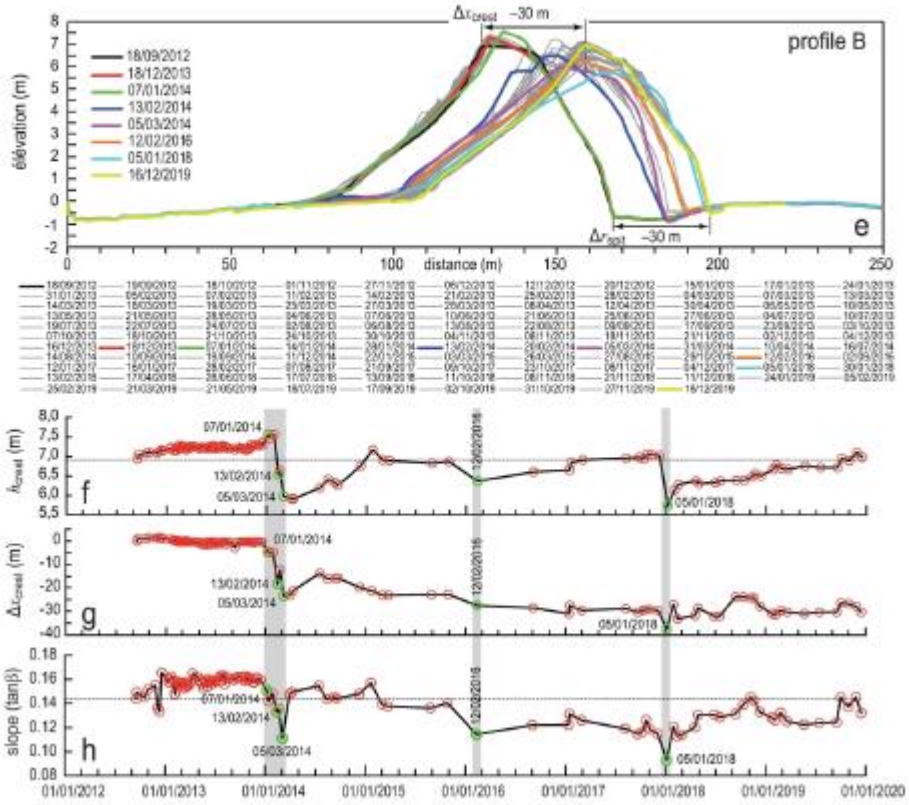

Figure_09b

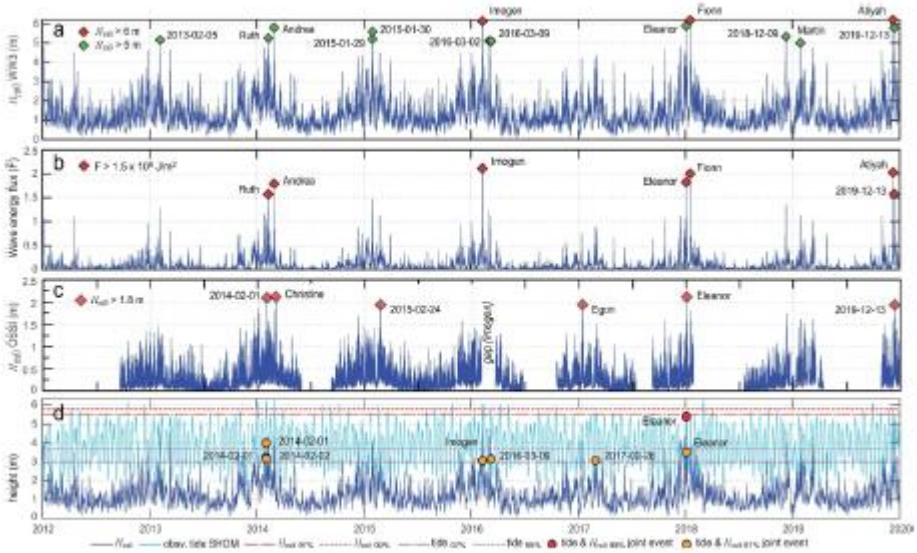

Figure_10

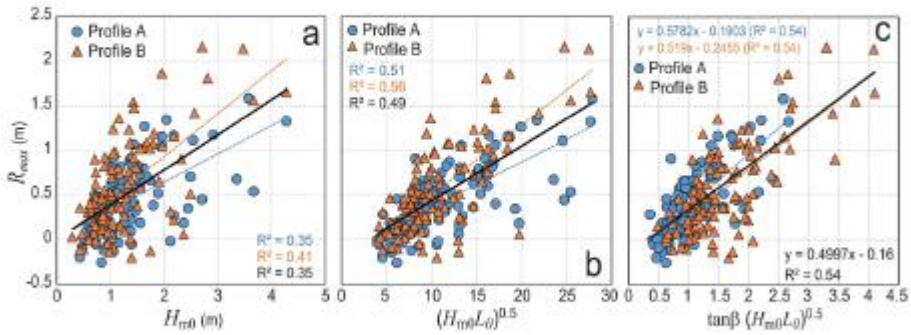

Figure_11

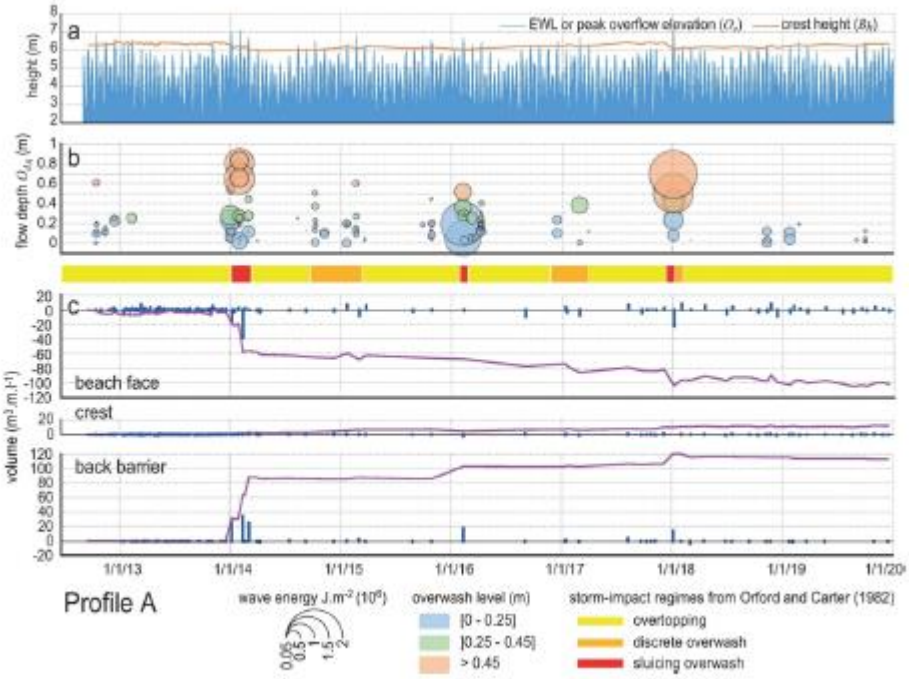

Figure_12a

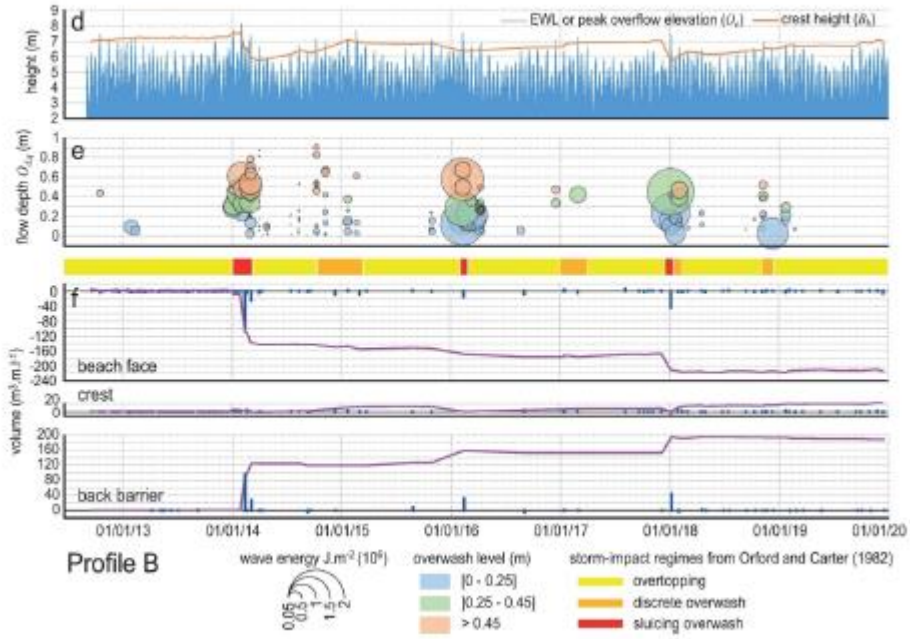

Figure_12b

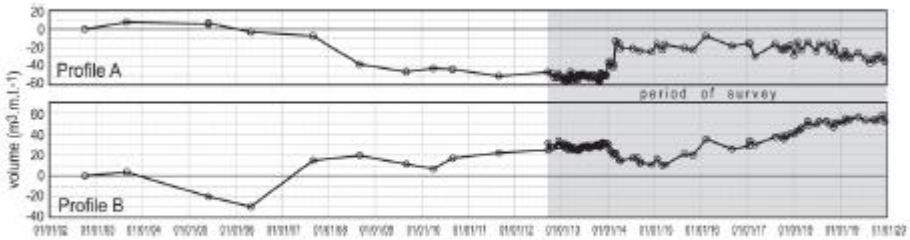

Figure_13

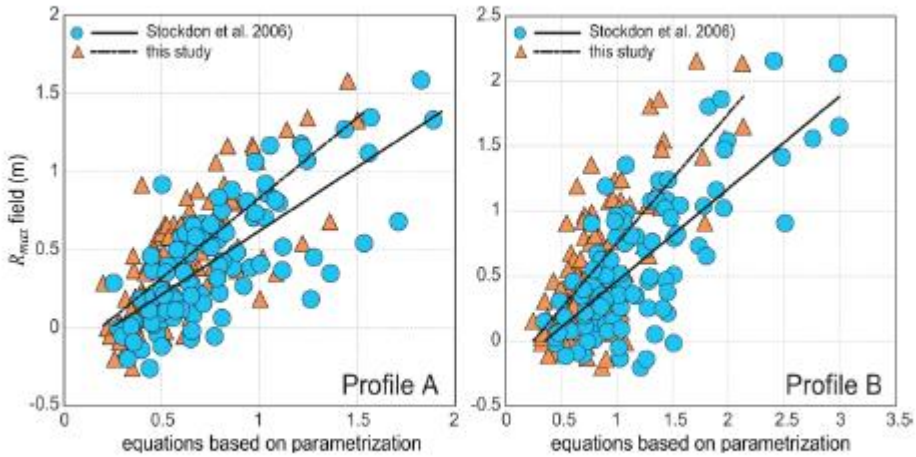

Figure_14